Experimental and Numerical Study of the effect of Gas-shrouded Plasma Spraying on Cathode Coating of Alkaline Electrolysis Cells

T. Liu[1], R. Reißner, G. Schiller and A. Ansar

Institute of Engineering Thermodynamics, German Aerospace Center,

Pfaffenwaldring 38-40, 70569 Stuttgart, Germany

Abstract

The aim of this work is to improve the performance of electrodes prepared via atmospheric plasma spray by means of gas shrouding which is expected to apparently reduce the oxygen content of the plasma plume and subsequently improve the coating quality. Electrodes with dual-layer coating for alkaline water electrolysis were deposited on Ni-coated perforated substrates. Microstructure and morphology were studied by SEM. Element content was measured by EDS. Enthalpy probe was employed for measuring plasma temperature and velocity as well as the gas composition. For verifying and better understanding the shrouding effect numerical calculation was carried out according to the experimental settings. Electrochemical test was carried out to validate the shrouding effect. The results showed slight protecting effect of gas shrouding on plasma plume and the final coating. Overall the dual-layer region, the measured oxygen fraction was 3.46% and 3.15% for the case without gas shrouding and with gas shrouding respectively. With gas shrouding the coating exhibited similar element contents as the coating sprayed by VPS while no obvious improvement was observed in the microstructure or the morphology. Evident electrochemical improvement was nevertheless achieved that with gas shrouding the electrode exhibited similar performance as that of the VPS sprayed electrode.

Keyword: atmospheric plasma spray; gas shrouding; alkaline water electrolyser; Computational fluid dynamics; hydrogen evolution reaction

[1] Corresponding author: Dr. Taikai Liu, email: taikai.liu@dlr.de, Tel: +49 711 6862 316

1 Introduction

As a clean energy carrier, hydrogen has drawn a lot of interests in industry and in academic research for overcoming the environmental and societal challenges caused by the global warming and climate change in recent years. And the most intensive concern is how to economically produce hydrogen with low emission or even without emission. It has been widely accepted to make use of the renewable energy to achieve the goal. As one of the most promising approaches to produce hydrogen alkaline water electrolysis (AWE) exhibits surprising potential of taking advantage of the renewable energy as well as the capacity to be integrated in large-scale energy storage (Ref 1–4). It has been intensively investigated to reduce the cost and to decrease the degradation of the electrodes throughout the development (Ref 1,5–7). The state-of-the-art of cathode material of AWE is Raney nickel which shows low over-potential and high current density for hydrogen evolution reaction (HER) (Ref 7–9). A lot of works have been published focusing on the processes to prepare cathodes with reasonable performance. Kjartansdóttir et al (Ref 3) tested a physical vapour deposited (PVD) Al/Ni electrode with over-potential of -1000 mV (vs SHE, standard hydrogen evolution) at 500 mA/cm^2 (1 M KOH at 25°C). Manazoğlu et al (Ref 10) reported an over-potential around -200 mV (vs SHE) at current density of 100 mA/cm^2 on an electroplated Ni/Mo electrode while Schiller et al (Ref 11,12) presented much better performance with an over-potential as low as -90 mV (vs RHE, reversible hydrogen evolution) at 500 mA/cm^2 based on VPS coated NiAlMo electrode.

Due to the outstanding performance and the moderate cost, VPS process is acceptable as one of the most reasonable methods to produce electrodes of alkaline electrolyser. However, the cost should be further reduced by turning from vacuum state to atmospheric state which is undoubtedly cost-saving and more flexible compared to VPS. The atmospheric plasma spray, however, brings critical problem of oxidization of the metal elements and then declines the performance of electrodes. For coping with this issue and maintaining the residual of metal elements as much as possible, protection of the plasma plume was proposed in form of gas shrouding as a compromise between protecting effect and cooling effect.

In present work, the effect of the gas shrouding on plasma plume and on electrode performance was experimentally and computationally investigated. Plasma gas composition, plasma temperature and plasma velocity were measured by enthalpy probe; and simulation was carried out by CFX (Ansys 17.0, Inc., US) considering the experimental condition. Electrodes were obtained by applying different shrouding conditions. And for comparison, a

VPS sprayed coating was also prepared. All coatings were examined by SEM for the microstructure and by EDS for the element contents. Electrochemical test was performed to determine the overpotential and obtain the voltage-current curve.

2 Methodology and installations

2.1 Experimental setups

2.1.1 Plasma spray installation

This work was carried out in a chamber which was able to be controlled in vacuum state or in atmospheric state by a vacuum pump/ventilation pump (see Fig. 1). The pressure of the chamber could be controlled either as low as 3000 Pa for VPS or be maintained at 1 atm. ($9.4x10^4$ Pa) for APS. Inside the chamber, a water-cooled F4 torch was installed to a precisely adjustable X-Y coordinate system (see Fig. 1(b)). The feedstock was perpendicularly fed to the plasma plume through an injector with 1.8 mm internal diameter being installed 3 mm upstream to the nozzle exit. The aim of the gas shrouding is to form a gas shield around the plasma plume to diminish the entrainment of cold ambient gas. Due to the net pressure limitation of the shrouding gas (maximum $3.76x10^5$ Pa), the shrouding head consists of 12-arranged shrouding nozzles was employed instead of annular type shrouding head to retain the initial momentum of the shrouding gas, as indicated in Fig. 2(b) and Fig. 2(c). The shrouding head was closely mounted to the outer surface of the plasma torch and therefore the unfavourable entering path of the ambient gas as indicated by P1 in Fig. 2(a) was occluded. In addition, a short solid shell was welded to the shrouding head with length of 15 mm and diameter of 70 mm that the entering path of ambient gas to the plasma was slightly modified as indicated by P2 in Fig. 2(a). The gas used for shrouding was argon with maximal net pressure of $3.76x10^5$ Pa. The input argon was delivered to the shrouding nozzles by two entrances as indicated in Fig. 2(b) and (c). In Fig. 2(d) the numerical model of a single shrouding nozzle was simplified to be a V-shape notch with an expanding angle of 30°.

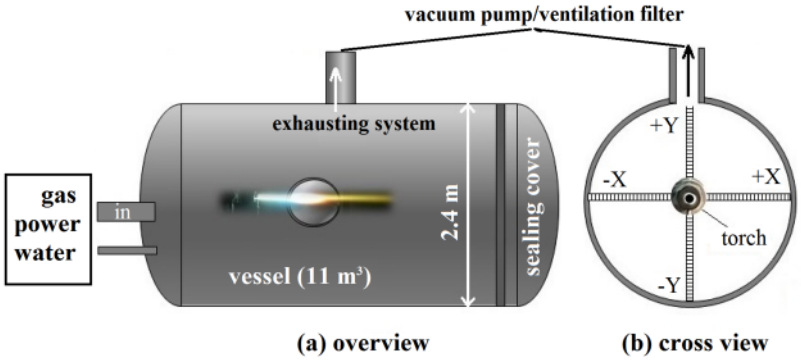

Fig. 1 the plasma spray installation with vacuum pump and ventilation pump

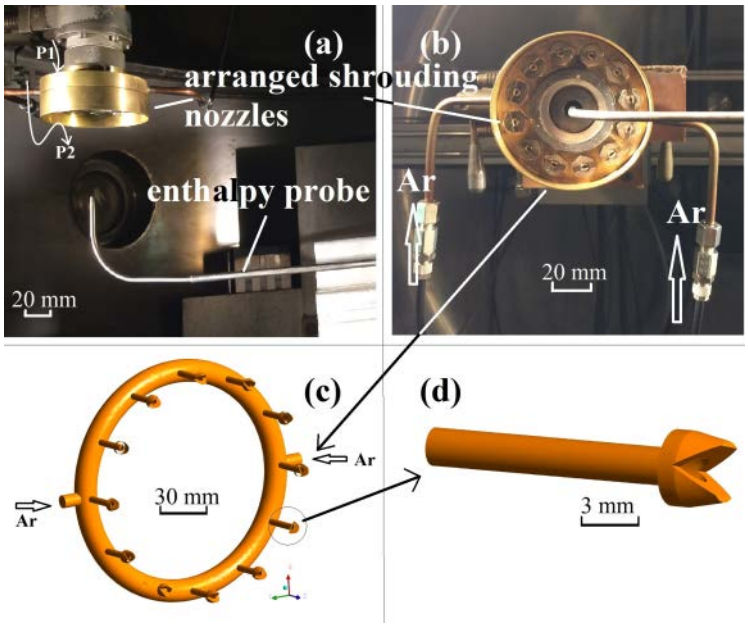

Fig. 2 installations of the arranged shrouding nozzles and the enthalpy probe: (a) top view; (b) front view; (c) model of the arranged nozzles with the gas delivering channel; (d) model of a single shrouding nozzle simplified for simulation

2.1.2 Enthalpy probe

A lot of works have been reported to successfully apply enthalpy probe to diagnose plasma plume with reasonable precision (Ref 13–17). In this work enthalpy probe measuring system from TEKNA (Québec, Canada) was employed to detect plasma gas composition, plasma temperature, plasma velocity and the density of plasma. The probe used was ENT 476 with orifice area of 1.27 mm^2 at the tip. The probe tip was placed on the centreline of the plasma

torch aperture and perpendicularly pointed to the centre of the plasma nozzle. Instead of moving the probe, the plasma torch was moved in resolution of 2 mm to adjust the measuring position for depicting the distribution of the gas composition as well as the temperature and the velocity of the plasma plume. According to the operating manual, the sampling rate of enthalpy probe was carefully adjusted to achieve isokinetic close to 1 as much as possible for reducing error.

2.1.3 Feedstock

The feedstock used in this work was commercially supplied NiAl (56/44 wt %) as the bonding layer and NiAlMo (39/44/17 wt %) as the top layer. The size distribution of the used powders was displayed in Fig. 3. The granularity test also indicated that the d_{50} was 15.43 µm and 16.67 µm for NiAl and NiAlMo respectively. The morphology of the two powders was shown in Fig. 4. Both of the two powders were spherical which shows better flow-ability and thus lower fluctuation in the powder feeding according to our prior work (Ref 18).

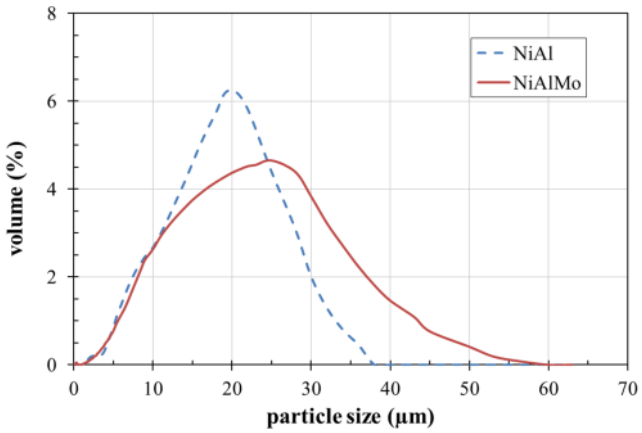

Fig. 3 the granularity of NiAl powder and NiAlMo powder

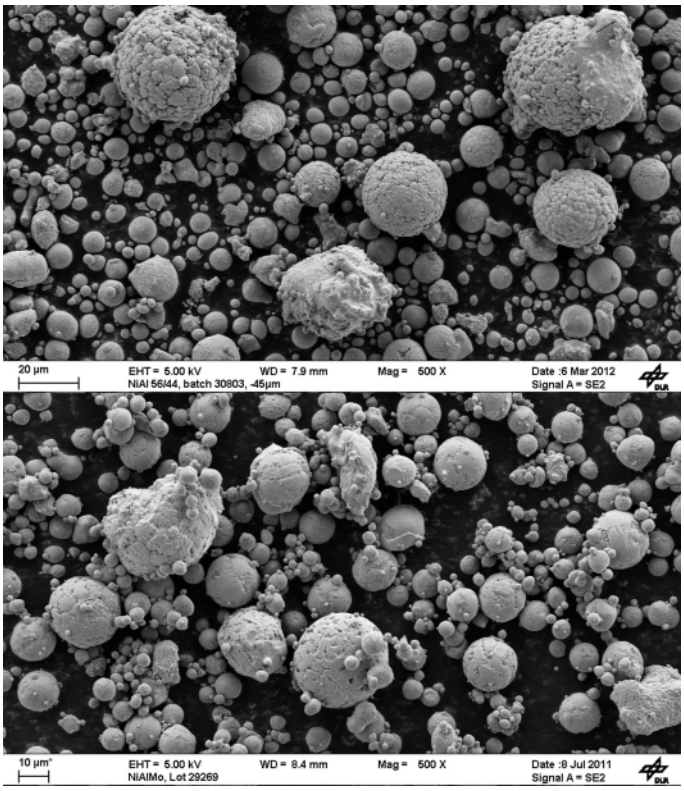

Fig. 4 the morphology of NiAl powder and NiAlMo powder

2.1.3 Samples preparation and procedure

Three samples were prepared with different pressures and different shrouding states (see Tab. 1). Sample 1 was sprayed in VPS (6000 Pa); sample 2 was obtained in APS (1 atm.) under argon shrouding with net pressure of 3.76×10^5 Pa (4 atm.); sample 3 was also prepared in APS but without argon shrouding. The substrates used were perforated stainless steel sheets with dimension of ϕ32 mm x 0.5 mm (see Fig. 5) on which a pure nickel layer was pre-coated with thickness of 36±6 µm. By means of image analysing the effective area of the substrates was estimated to be 555 mm^2. After sandblasting, 5 layers of NiAl were firstly sprayed and then 10 layers of NiAlMo were deposited on the NiAl layer of each sample.

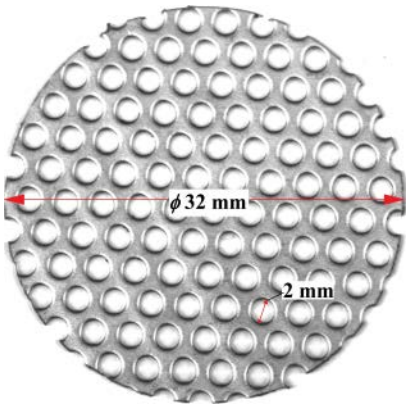

Fig. 5 the perforated stainless steel sheet used as substrate in this work

2.2 Numerical settings

2.2.1 Assumption and governing equations

For verifying the effect of gas shrouding, simulations were carried out focusing on the plasma plume behaviour as well as the ambient gas behaviour. The behaviour between plasma gas and the arc generated between anode and cathode was not interesting in this work and thus not mentioned. The magnetic force on particles and the current density on electrodes were also not interesting for this work. The plasma gas was considered as hot fluid with constant initial velocity and temperature. This simulation was also based on the following assumption: the plasma is in equilibrium; the profile of temperature and velocity of the plasma plume is in the form of Gaussian distribution; the plasma gas is a mixture of Ar and H_2; all solid parts are rigid and thermal insulator; the cooling effect of the solid part was not considered; the entrained air was a mixture of 79% N_2 and 21% O_2; the properties of the ambient gas was determined by the instant temperature according to the predefined data base.

Three governing equations were used (Ref 19):

The conservation of mass: $\nabla \cdot (\rho \boldsymbol{U}) = 0$ (1)

The conversation of momentum: $\nabla \cdot (\rho \boldsymbol{U}\boldsymbol{U}) + \nabla p - \nabla \vec{\tau} = 0$ (2)

The conservation of energy: $\nabla \cdot (\rho \boldsymbol{U} h) - \alpha \nabla^2 T = 0$ (3)

where ρ denotes the density, kg/m^3; $\boldsymbol{U}$ gives the vector of velocity, m/s; p means the pressure, Pa; τ indicates the stress tensor, Pa; T presents the temperature, K; h gives the enthalpy, J/kg; α is the thermal conductivity, W/m^{2}K.

For closing the equations, the stress tensor τ in equation 2 is given as follow:

$$\vec{\tau} = \mu\left[(\nabla \boldsymbol{U} + \nabla \boldsymbol{U}^T) - \frac{2}{3}\nabla \cdot \boldsymbol{U} I\right] - pI \qquad (4)$$

where μ gives the viscosity, Pa.s; and I presents the unit tensor calculated as product of $A_{ik}A_{jk}$ which are two matrices automatically produced during the iteration (Ref 20).

Standard k-ε model was employed for calculating the turbulence kinetic energy k and the rate of the dissipation ε according to the following equations (Ref 21):

$$\nabla \cdot (\rho k \boldsymbol{U}) = \nabla \cdot \left[\left(\mu + \frac{\mu_t}{\sigma_k}\right)\nabla k\right] + G_k + G_b - \rho\varepsilon - Y_M \qquad (5)$$

$$\nabla \cdot (\rho \varepsilon \boldsymbol{U}) = \nabla \cdot \left[\left(\mu + \frac{\mu_t}{\sigma_\varepsilon}\right)\nabla \varepsilon\right] + C_1 \frac{\varepsilon}{k}(G_k + C_3 G_b) - C_2 \rho \frac{\varepsilon^2}{k} \qquad (6)$$

where G_k presents the generation of the turbulence kinetic energy from the mean velocity gradients; G_b presents the turbulence kinetic energy generated by buoyancy; Y_m gives the dedication of the fluctuating dilatation in the compressible turbulence to the dissipation rate; C_1, C_2 and C_3 are constants which are also able to be defined by user; μ_t denotes the turbulent viscosity which can be calculated as product of $0.09\rho k^2/\varepsilon$; δ_k and δ_e are the turbulent Prandtl numbers for k and ε with default value of 1 and 1.3 respectively (Ref 20).

Simulation gives more intuitional results compared to the experimental measuring; however it must concede that the precision of simulation is highly depended on the calculation settings. It is really hard to say how close the simulation is to the truth before knowing what the exact truth is. For example, when the reaction between the primary gas and the secondary gas is the interesting point and the simulation of his work only focuses on the gas distribution, it may say this work is completely a flaw. Thus, it is necessary to point out that in this work the gas distribution and the plasma property (temperature, velocity and density) are the only interesting points. Then it is reasonable to claim whether the simulation works carried out based on the above assumptions and settings are close to the observe.

2.2.2 Computational domain and conditions

This simulation focused on the behaviour of plasma plume and the effect of gas shrouding. Thus the plasma was simplified as hot gas with given temperature and velocity when entering the computational domain through the plasma inlet as indicated in Fig. 6. The plasma inlet was created based on the F4-VB torch with adiabatic wall. The computational domain was mainly composed of the plasma nozzle, the shrouding system and a cylinder with dimension of ϕ120 mm x 200 mm for the progress of the off-gas.

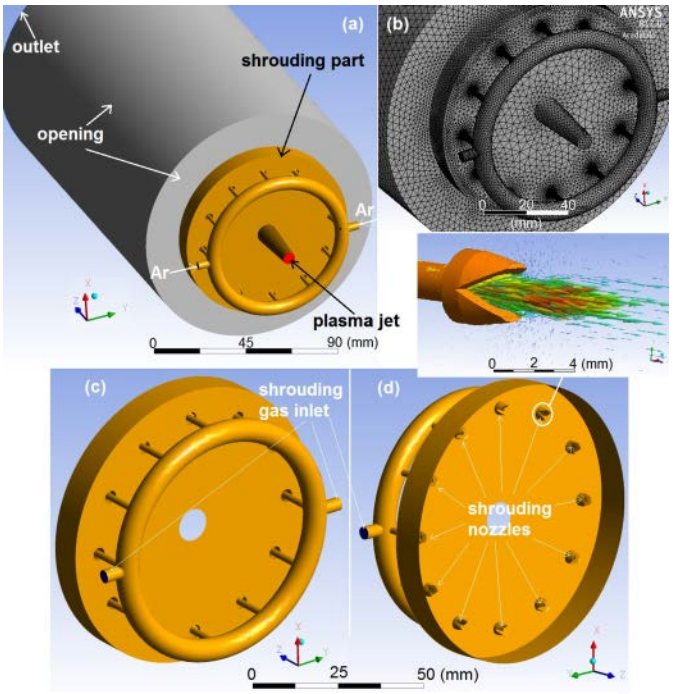

Fig. 6 model of simulation: (a) the mesh; (b) the model with 12-arranged nozzles for shrouding; (c) illustration of the result display and (d) a single nozzle for shrouding

For evaluating the entrainment of ambient gas in the plasma plume, gas composition at different boundaries was predefined with volume fraction of corresponding component: the plasma inlet was defined with 100% plasma gas and 0% air; the shrouding gas inlet was defined with 100% argon; the opening boundary was defined as 90% air and 10% plasma gas; and the outlet was empirically defined as 50% air and 50% plasma gas considering the distance and the back-flow of off-gas. The temperature of the ambient gas at the opening and the outlet was defined at 320 K while the shrouding gas was set at 300 K. The distributions of

the inlet temperature for the plasma gas were given as function of coordinate *x* and *y* as follows:

$$T(x,y) = T^0 \times e^{c(x^2+y^2)/r^2} \quad (7)$$

Where T^o presents the given temperature, 15000 K; *c* is the constant with value of -2.1; *r* gives the orifice radius of the plasma torch, 0.003 m; *x* and *y* indicate the coordination, m.

The plasma inlet was defined as a mass inlet with flowrate of 0.00122183 kg/s which was calculated according to the total flow rate of plasma gas listed in Tab. 1. Moreover, because the plasma gas was simplified as a mixture of 90% argon and 10% hydrogen, the properties of the plasma gas were thus considered as 90% from argon and 10% from hydrogen.

Tab. 1 operating parameters and shrouding state

No.	I (A)	Ar (SLM)	He (SLM)	H_2 (SLM)	pressure (Pa)	shrouding	distance (mm)
1	420	45	10	4	$6x10^3$	0	80
2	420	45	10	4	$9.4x10^4$	1	80
3	420	45	10	4	$9.4x10^4$	0	80

3 Results and discussions

3.1 The effect of gas shrouding on the plasma plume

The plasma plume was radially and axially measured by enthalpy probe. By vertically adjusting the plasma torch (*Y*+/-) it is able to determine the distribution of temperature, velocity and the density (TVD) of the plasma plume. And it is also able to obtain TVD of the plasma plume at different axial standings by moving the probe tip of enthalpy probe (*Z*+/-). In simulation the plasma's TVD was able to be easily exported according to a predefined line. Consequently, plots of measurements and simulations were jointly presented in Fig. 7 with lines presenting the simulation results (T_sim_SH0, T_sim_SH4…) and the discrete markers

indicating the experimental results (T_exp_SH0, T_exp_SH4…). The denotation “SH0” mentioned here signified no gas shrouding and “SH4” indicated gas shrouding with pressure of 4 atm. ($3.76x10^5$ Pa). Accordingly, two aspects were clearly observed from Fig. 7: first, the gas shrouding evidently affected the plasma plume; second, the simulation fit the experiment well. Both experiment and simulation indicated that the shrouding gas could bring cooling effect to the plasma plume and slight reduction of the plasma temperature was observed in the downstream region starting from Z= 70 mm as displayed in Fig. 7(a); moreover, the plasma density was found to become higher which means a decrease of temperature. While, as shown in Fig. 7(b) it is hard to distinguish the shrouding effect on plasma velocity that with or without gas shrouding the plasma velocity were found to be more or less the same.

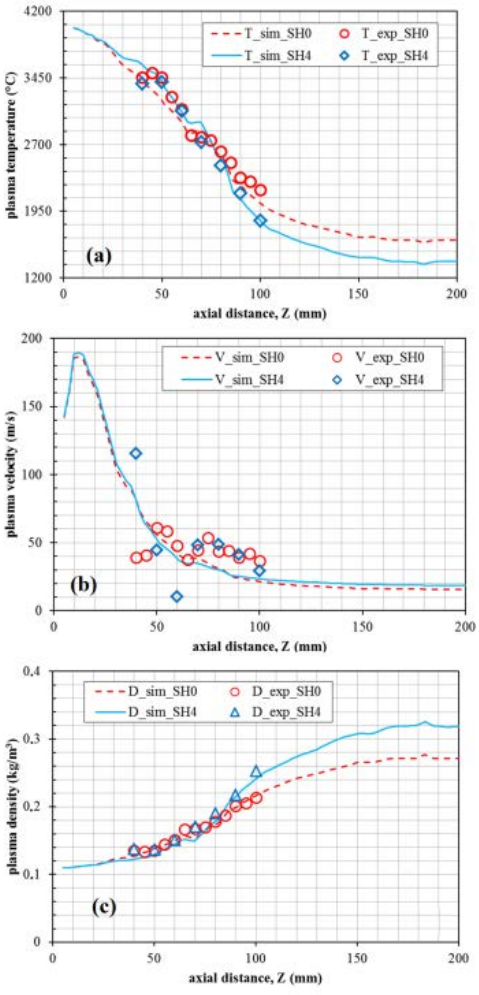

Fig. 7 measured and simulated characteristics of the plasma jet: temperature (a), velocity (b)

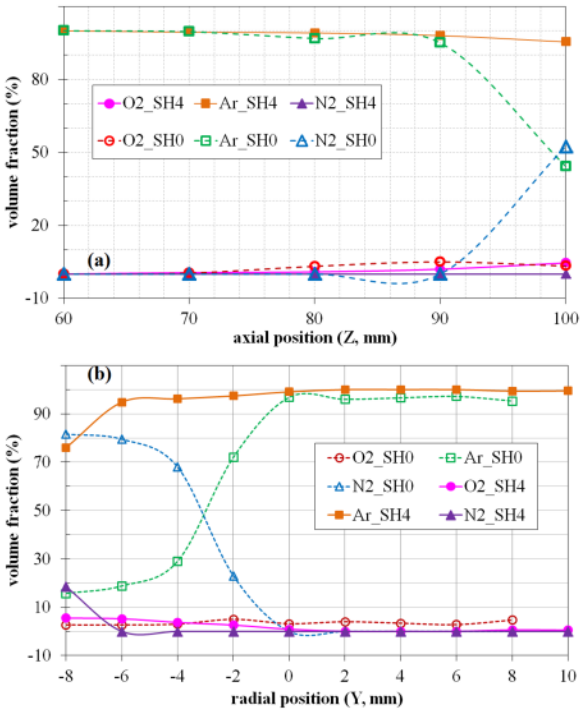

Fig. 8 measured gas composition along axial position (Y=0 mm) (a) and against the radial

and density (c) displacement (Z=80 mm) (b)

In addition, the gas shrouding also brought significant effect to the composition of plasma as well as the surrounding gas. As shown in Fig. 8, the measured axial and radial distributions of O_2-N_2-Ar were depicted with dashed lines and void markers for the case without gas shrouding; the plots with solid lines and filled markers represented the case with gas shrouding. It can be found that with gas shrouding the axial region between 70 mm and 100 mm was well protected to have higher argon fraction and lower oxygen fraction (see Fig. 8(a)). At the spraying distance (80 mm), the oxygen fraction was decreased from 3.2% to 0.9% measured by enthalpy probe; while the argon fraction was increased from 96.8% to 99.1%; and more surprisingly N_2 was detected to decrease from 52% to 0 by applying gas shrouding. Radially, the argon-rich region around the plasma plume was obviously expended by the shrouding gas that the edge has been extended from Y=-4 mm to Y=-10 mm (see Fig. 8(b)). Without gas shrouding, the fraction distributions of argon and nitrogen were found to have a crossover at about Y=-7 mm; while with gas shrouding, the crossover was predicted at about Y=-13 mm.

Moreover, the shrouding effect was also confirmed by the simulation results. As displayed in Fig. 9(a) and Fig. 9(b), with gas shrouding the gas distributions were evidently affected that in axial direction (see Fig. 9(a)) the plasma plume between Z=50 mm and Z=170 mm was protected to have more argon and with less air (less O_2 and N_2). At Z=80 mm, the calculated fraction of oxygen reduced from 7.5% to about 2.4%; and nitrogen was restricted with volume fraction as low as 9% which was only one third of that without gas shrouding; meanwhile, the fraction of argon was increased from 57% to 83%. It is clearly observed from Fig. 9(a) that without gas shrouding the curve Ar_SH0 intersected the curve N_2_SH0 at about Z=100 mm while with shrouding the crossover was extended to Z=150 mm. In parallel, the simulation also gave reasonable results about the radial gas distribution that the shrouding gas was able to protect the spraying by shielding the plasma plume from the air. However, due to the simplification of the calculating models, gap might exist between the simulation and the experiment. But at least it gave the possibility to justify the effect of the gas shrouding on the plasma plume.

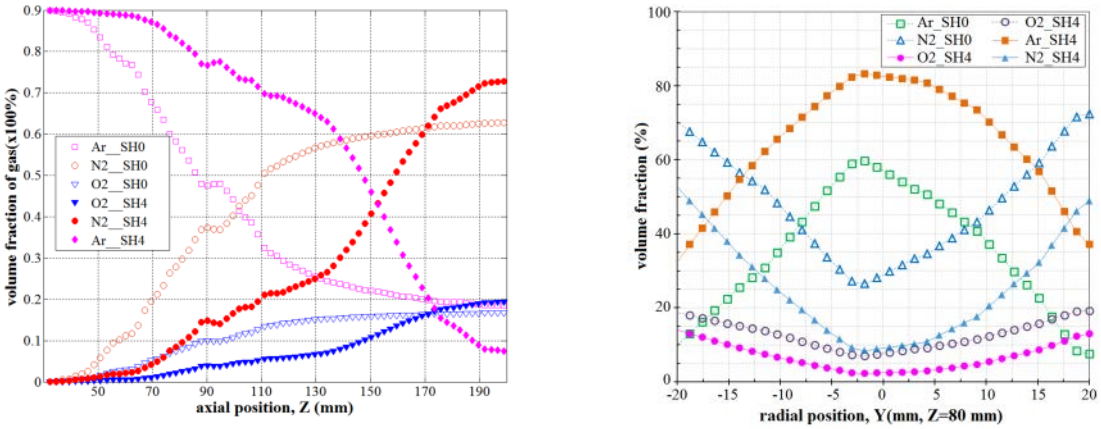

(a) (b)

Fig. 9 the distribution of Argon, oxygen and Nitrogen axial-Z (a) and radial-Y (b)

Additionally, the filled contour of oxygen distribution provided more intuitive evidence about the shrouding effect. As shown in Fig. 10, the oxygen distributions on three selected planes (Y=0 mm, Y=5 mm and Y=10 mm) were found with dramatic differences. By applying gas shrouding, the plasma plume was found to become radially wider and axially shorter with more region being protected from oxygen. Moreover, as depicted in Fig. 10, the shrouding gas released by the shrouding nozzles was simultaneously drawn toward the plasma core due to the low pressure generated by the expansion of the plasma plume. Consequently, the gas from the 12-arranged nozzles finally formed an annular gas shield that prevents the entrance of the cold ambient gas into the hot plasma and thus can keep the inside plasma plume at low oxygen content. As shown in Fig. 11(a) and Fig. 11(b), without gas shrouding the majority of the slice at 10 mm away from the plasma torch exit was oxygen-rich; while in Fig. 11(c) and Fig. 11(d) the entrainment of oxygen to the shrouded region was evidently inhibited and resultantly the argon-rich region at the centre was enlarged.

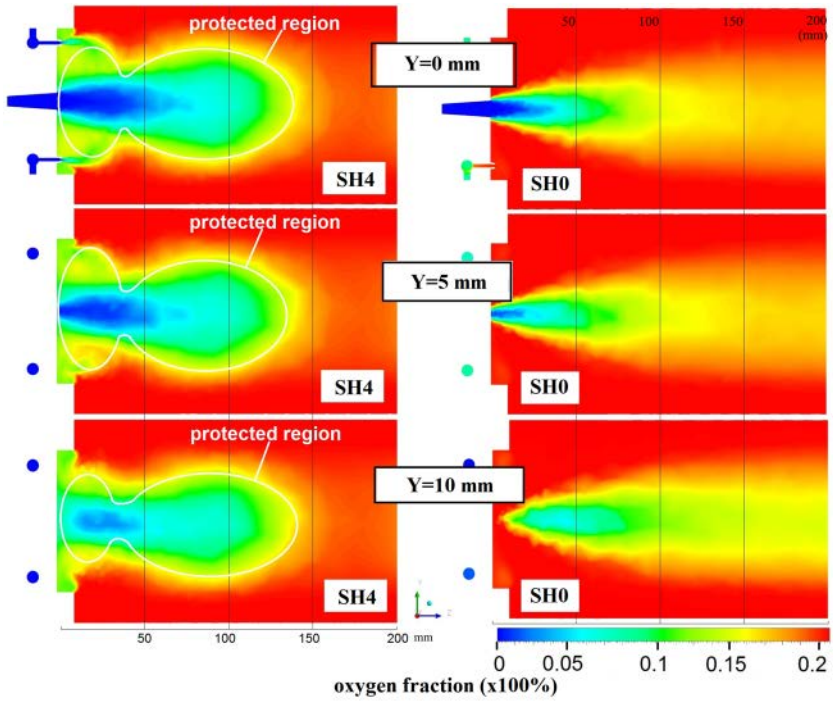

Fig. 10 the simulated distribution of oxygen on the selected planes

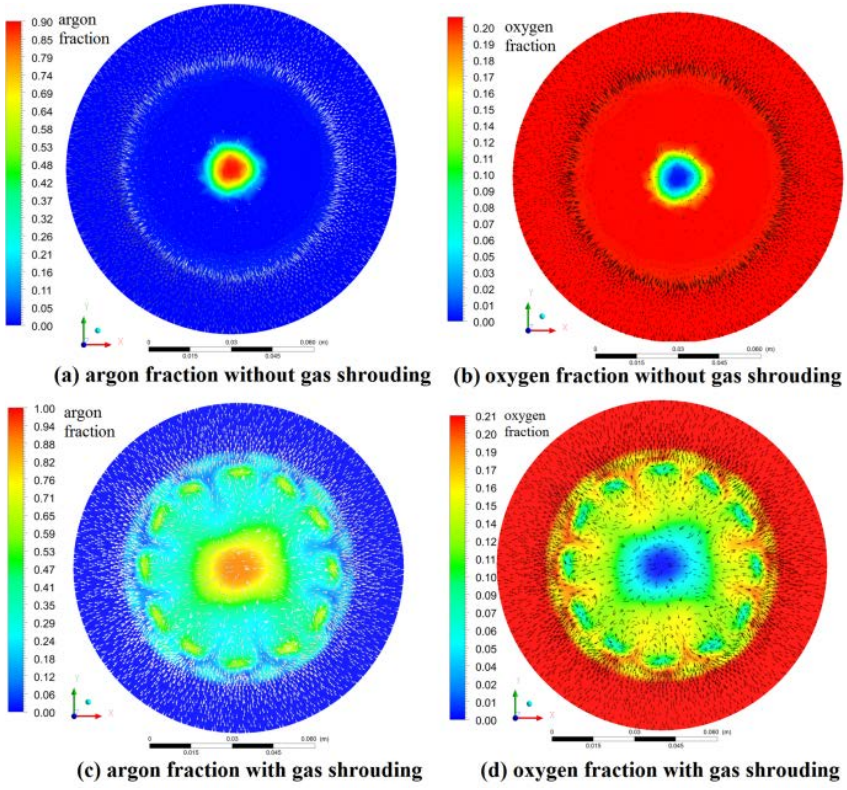

Fig. 11 argon fraction and oxygen fraction at selected slice (10 mm away from the plasma torch exit) without gas shrouding (a) and (b), with gas shrouding (c) and (d)

Unfortunately it is impossible to completely eliminate the entrainment of the cold ambient gas due to the existence of intervals between the arranged shrouding nozzles (see Fig. 6 and Fig. 11). As mentioned in section 2.1 the shrouding head with 12-arranged nozzles was applied as a compromise between the shrouding effect and the cooling effect. It is indubitable that the stronger the shrouding effect is, the lower the temperature becomes. The shrouding effect was dominated by the flowrate of the shrouding gas and the momentum that the more the shrouding gas used, the more intensive the gas shield will be; and the higher the momentum of the shrouding gas is, the stronger the gas shield will be. Compared to the current 12-arranged shrouding nozzles, an annular shrouding nozzle is able to provide gas shield without any interval. However, it requires higher shrouding pressure to obtain comparable protecting effect. For retaining high enough momentum of the shrouding gas to withstand the entrainment of the cold ambient gas, the shrouding pressure has to be much higher than 4 atm. ($3.76x10^5$ Pa). Then, the plasma plume is able to be better protected by the strong gas shield while the plasma temperature will be inevitably intensely reduced which is detrimental to the coating property. Additionally, the maximal net pressure in this work was limited to $3.76\ x10^5$ Pa that it is impossible to achieve a higher pressure. Therefore, the module with 12-arranged-nozzles was finally employed in this work and it showed expected protecting effect to the plasma plume even with unfavourable intervals between nozzles as indicated in Fig. 11(c) and Fig. 11(d).

The effect of gas shrouding on the in-flight particles was not investigated. But it can be easily foreseen that in the protected region the in-flight particles have more chance to be completely melted and protected from being oxidized while no evident change in particle velocity can be induced due to the ignorable change in the plasma velocity. However, out of the protected region, the plasma plume is continuously cooled by the shrouding gas and the ambient gas that may cause increase of unmolten particles and thus low deposition efficiency. Unfortunately, more details of in-flight particles are not available in this work.

3.2 The effect of gas shrouding on coatings characteristics

For estimating the effect of gas shrouding on coating characteristics, microstructure and element composition of coatings have been analysed by means of SEM and EDS. All samples

consisted of two coatings: NiAl coating which was directly deposited on the pre-coated Ni surface and NiAlMo coating which was subsequently sprayed onto the NiAl coating. The addition of Mo is expected to improve the catalytic activity and the durability of electrode. It is well accepted that the electrode activity is highly dominated by the effective surface area. For achieving high enough surface area, a chemical etching process should be executed. After leaching, most of the leachable Al components will be dissolved in the electrolyte in form of $KAl(OH)_4$ and resultantly both layers become highly porous. It has been reported that after leaching the active electrochemical surface area can be 543 times of the geometrical surface area of the substrate (Ref 3). Although the active surface area of electrode was not measured in this work, the leaching effect is apparent. It is clear that the fraction of leachable Al in the as-sprayed coatings gives significant influence on the active surface area of the electrode.

As displayed in Fig. 12, before leaching, sample 1, prepared by VPS, was obviously denser and thicker than sample 2 and sample 3. And sample 2 and sample 3 exhibited similar structures with comparable pores deeply trapping in NiAl layer. As a result of gas shrouding, sample 2 presented a moderate mass percent of oxygen with a reduction of 0.31% compared to 3.46% the oxygen content in sample 3 (see Tab. 2). The content of Al in sample 2 was found to be higher than that of sample 3. It meant that after activation sample 2 might have more active surface area than sample 3. In addition, the content of Ni in sample 2 was found to be 48.83% which is very close to that of sample 1 while sample 3 consisted of higher Ni with mass percent of 51.56%. However, the content of Mo was almost the same between sample 1 and sample 2 with value of 10.64% and 10.72% respectively. While the Mo content of sample 3 was slightly lower with value of 9.87%.

Tab. 2 mass percent of elements of as-sprayed coatings in different cases

No.	Spray condition	Mass percent (%)			
		O	Al	Ni	Mo
1	VPS	1.8	38.62	48.94	10.64
2	Shrouded APS	3.15	37.30	48.83	10.72
3	Normal APS	3.46	35.11	51.56	9.87

Moreover, regarding the content of Al in the two feedstocks (NiAl 56/44 and NiAlMo 39/44/17), it can be estimated that the global content of Al in the as-sprayed coatings was about 44%. And thus it was possible to further evaluate the loss of Al during the spraying for each sample: 5.38% in sample 1, 6.7% in sample 2 and 8.9% in sample 3. The cause of the loss was mainly due to the vaporization of Al during the flight owing to the relatively low boiling point of Al (2327°C) and the oxidization of Al to Al_2O_3 which needs much higher temperature to be softened or melted (2054°C). Therefore, as conclude of this part, executing gas shrouding brought slight reduction of oxygen in the coating and it was useful for retaining Al. With the highest oxygen content and the lowest Al percent, sample 3 was supposed to have the lowest electrode performance.

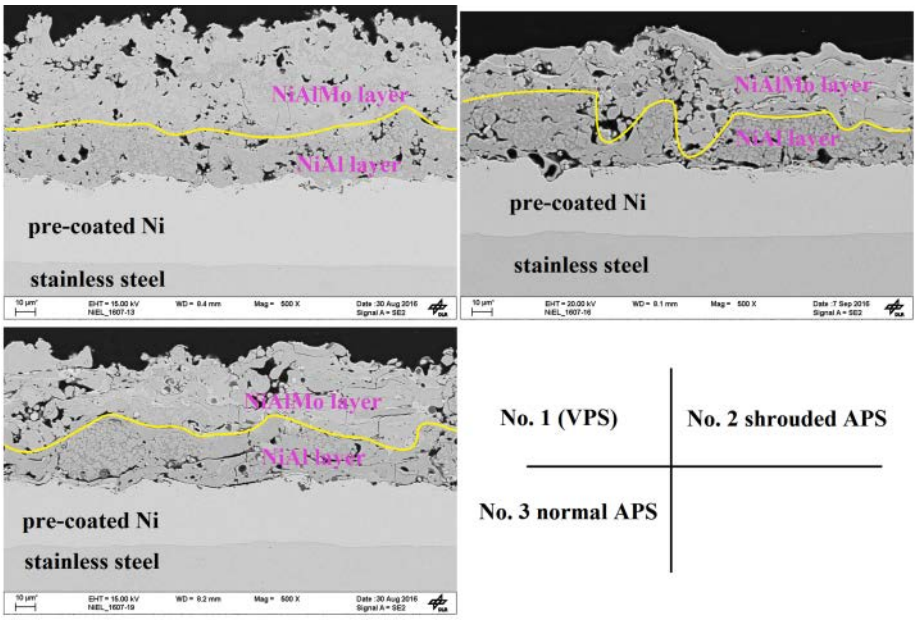

Fig. 12 microstructure of as-sprayed coatings in different cases

3.3 Electrode performances

The well prepared electrodes were tested as half-cells with setup developed at DLR. The as-sprayed electrodes were firstly activated in a mixture of KOH solution and K-Na-Tartrate-Tetrahydate for 24 hours at 80°C and then transferred to the test platform in 30wt% KOH at 70°C at ambient pressure to measure the electrochemical performance. A conventional three-electrode cell was used including a working electrode, a reference electrode and a counter electrode. The reference electrode used is a reversible hydrogen electrode (RHE) (Gaskatel GmbH) (Ref 22), which allows the direct measurement of overpotential in strong alkaline

electrolyte without suffering the influence of the high pH. Reversible Hydrogen Electrodes is in the same solution as the sample which means that the equilibrium potential of Hydrogen evolution is nearly constant with quite slight variation determined by temperature and pH value. And Ni was used as the counter electrode for balancing the reaction occurred on the working electrode. The generated gas was released to air by carefully excluding any potential explosion.

3.3.1 Overpotential

For comparing the electrode performances, typically, working voltage at 0.5 A/cm^2 was collected. As the reference electrode could not be directly mounted on the surface of the working electrode, a voltage drop might be presented with unexpected variation. For compensating the voltage drop IR correction was applied with “I” signifying the current and “R” indicating the high frequency impedance between the working electrode and the reference electrode. The IR-corrected overpotential was given in Fig. 13 with assumption that the overpotential is 0 V when the measured potential is 0 V vs RHE.

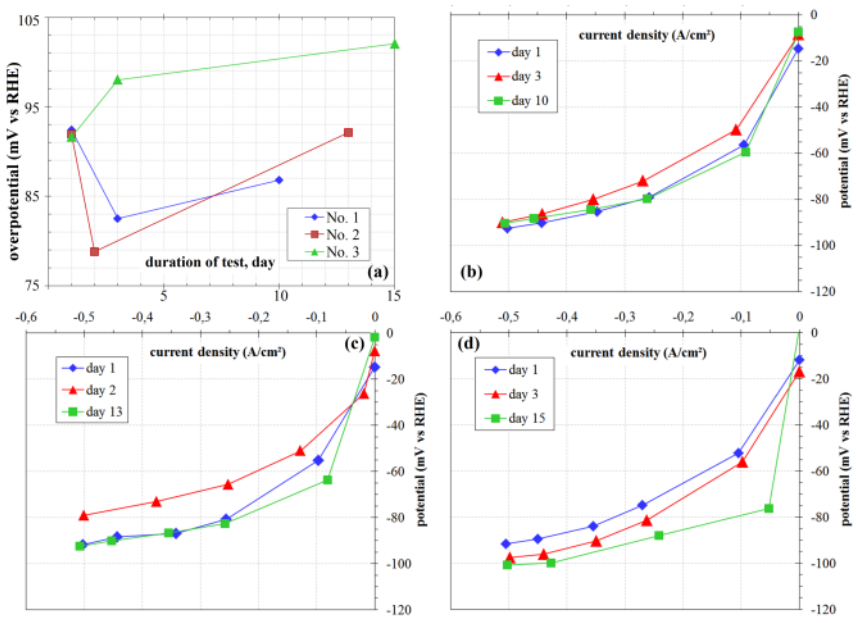

Fig. 13 electrochemical test results: (a) overpotential of electrodes operated at 0.5 A/cm²; (b) CV curve of sample No. 1 (VPS); (c) CV curve of sample No. 2 (shrouded APS); (d) CV curve of sample No. 3 (normal APS)

As displayed in Fig. 13(a), at the beginning, all samples showed comparable overpotential which meant that all electrodes were equally activated to have similar amount of electrochemical active surface area. After three days of test, the overpotentials of sample 1 and sample 2 were found to become even lower than that at the first day which might be due to the reactivation effect of the electrolyte solution that the residual Al components with low leachability can be continuously etched by the testing electrolyte. Conversely, sample No. 3 was found to have overpotential slightly higher than that at the first day which indicated the onset of degradation. At the end of the test, sample No. 2 presented overpotential as low as 92 mV while sample 3 gave an overpotential 10 mV higher. Undoubtedly, electrode No. 1 was the best with the lowest overpotential (87 mV vs RHE). It is clear that with gas shrouding, the overpotential of APS sprayed electrode was slightly optimized to be close to that of the VPS sprayed electrode. Without gas shrouding, the APS sprayed electrode exhibited the lowest performance, however the difference was just minor.

Short G. D. et al (Ref 23) have pointed out that the overpotential is a compound of activity, concentration and resistance. Activity represents the surface state of the electrode after chemical activation which decides the starting point of the overpotential; concentration denotes the concentration of conducible ions in the electrolyte solution which determines how strong the current density can be; finally the resistance stands for the resistance of charge transfer in the electrolyte. In the present work, the similar starting point of the overpotential means that all samples were comparable in the activity. In addition, the testing electrolyte for all samples was procedurally and chemically the same that all samples were expected to consist of same ion transfer resistance. Thus, it can infer that the overpotential difference between sample No. 1 and No. 2 or No. 3 is mainly due to the different oxygen content that lower oxygen means more leachable Al component and then higher active surface area. It also gives the reason of a 5 mV margin of sample No. 2 compared to sample 3. In spite of that, sample No. 2 and No. 3 were morphologically similar. Hence, it can foresee that sample No. 2 will be gradually and continuously approaching to sample No. 3 in performance.

3.3.2 Stability test

Very long-term stability tests of these electrodes were not available, but as a compromise, electrodes were tested for 10-15 days. As displayed in Fig. 13 (b, c and d), the current-voltage plots for each case were parabolic that the potential was approaching to an extremum around 100 mV vs RHE with the increase of current density to 0.5 A/cm^2. The overpotential was always around 90 mV for both No.1 and No. 2 even after 10 days operation. The current-

voltage plots of day 1 and of day 10 were practically identical for sample No. 1. Similarly, the plots of day 1 and day 13 for sample No. 2 were also fairly close to each other. It means that the degradation after 10-15 days operation was insignificant for both No.1 and No. 2. Conversely, sample No. 3 was found with evident degradation between the three current-voltage plots. Therefore, it is evident that sample No.1 (VPS) and No. 2 (shrouded APS) presented better stability than sample No. 3.

3.3.3 Tafel slope

It has been well accepted that the mechanism of HER is mainly composed of the following three steps (Ref 2, 10, 24-25):

(1) Volmer reaction: $H_2O + \mathbf{e}^- + M \leftrightarrow M{-}H_{ads} + OH^-$

(2) Heyrovsky reaction: $M{-}H_{ads} + H_2O + \mathbf{e}^- \leftrightarrow H_2 + OH^- + M$

(3) Tafel reaction: $2M{-}H_{ads} \leftrightarrow H_2 + 2M$

where M presents the adsorption site of the electrode; H_{ads} denotes the adsorbed hydrogen atom. During the Volmer reaction hydrogen ion is adsorbed by the metallic electrode and reduced to hydrogen atom by accepting an electron; the Heyrovsky reaction stands for the electron desorption and Tafel reaction involves the H recombination. Tafel slope is usually employed to distinguish the rate-determining step: the Tafel slopes will be -120 mV/decade, -40 mV/decade or -30 mV/decade when Volmer reaction, Heyrovsky reaction or Tafel reaction is rate-determining step (Ref 2, 10, 26-27).

As provided in Tab. 3, the Tafle slope was calculated based on the CV curve in Fig. 13 according to the Tafel equation, $\eta = a + b \log|J/\mathrm{Acm}^2|$ where η is the overpotential, a is the exchange current density term, b is the Tafel slope and J is the current density (Ref 26). On the first day, all samples presented comparable Tafel slope with value in range of -50~-58 mV/decade which means the Heyrovsky (-40 mV/decade) is the rate-determining step for all three samples. The deviation of Tafel slope from the theoretical value is owing to the formation of hydrides on the absorbing site. With Tafel slope of -50 mV/decade all catalysts are assumed to be completely occupied by the adsorbed H atoms. The new formed hydrogen gas stacks at the interface (solid-electrolyte) and obstructs the contact between the adsorbed H atoms and the electrolyte. Therefore, the hydrogen evolution has been impeded (Ref 10, 26-

28). In addition, it is evident that with value of -50 mV/decade and -51 mV/decade sample No. 1 and No. 2 showed similar mechanism for hydrogen evolution while sample No. 3 suffered from a slightly higher HER resistance with Tafel slope of -58 mV/decade. That means the gas-shrouded sample is electrochemically better than the normal APS sprayed sample, and yet the rate-determining step to the HER is the same for the three samples.

Tab. 3 Tafel slopes of samples prepared by different processes

No. 1	No. 2	No. 3
-50 mV/dec. @day 1	-51 mV/dec. @day 1	-58 mV/dec. @day 1
-25 mV/dec. @day 3	-47 mV/dec. @day 2	-64 mV/dec. @day 3
-17 mV/dec. @day 10	-35 mV/dec. @day 13	-40 mV/dec. @day 15

Moreover, on the 3rd day and the 10th day, No. 1 showed a decrease of Tafel slope to -25 mV/decade and -17 mV/decade respectively that the rate-determining steps of HER thus turned to be Tafel reaction (-30 mV/decade). Sample No. 2 was also found with decreased Tafel slope of -47 mV/decade (day 2) and -35 mV/decade (day 13) which is still in range of Heyrovsky reaction. While, sample No. 3 showed increased Tafel slope of -64 mV/decade on the 3rd day and then a decrease to -40 mV/decade was observed on day 15. Decrease or increase of Tafel slope during the test indicates change in the electrochemical active surface area of the tested electrode. In present work, the electrochemical activity of electrodes was gradually decayed during the test mainly due to the loss of active surface area and thus caused increase of the overpotential. It has been reported by Kjartansdóttir (Ref 3) that the residual Al components (Ni_2Al_3, NiAl, Ni_3Al…) will be continuously etched by the electrolyte, e.g. $Al_3Ni_2 + 3\ OH^- + 9H_2O \rightarrow 3\ Al(OH)_4^- + 4.5\ H_2 + 2Ni$ (Ref 3). And consequently, the precipitation of Aluminium hydroxide will arise due to the absence of K-Na-Tartrate-Tetrahydate which was only used during the activation procedure to prevent the formation of precipitable Aluminium hydroxide according to the reaction: $Al(OH)_4^- \rightarrow Al(OH)_3 + OH^-$. Consequently, the Nano-/micro pores produced by leaching were slowly clogged and the active electrochemical surface was resultantly decreased. In addition, the formation of Ni

Hydroxide was also expected to be progressively proceeded and to accessorily cause the loss of active electrochemical surface area (Ref 29).

Another work has been reported by Fletcher et al (Ref 30) that the Tafel slope can be as low as -20 mV/decade when more electrochemical and chemical steps are involved. As mentioned above, the continuous forming of Al hydroxide and Ni hydroxide will take place at the electrode-electrolyte interface as well as the HER. The charge transfer coefficient, who determines the Tafel slope, thus can be largely varied. Regarding the decrease of overpotential in Fig. 13 (a) and the decrease of Tafel slope in Tab. 3, sample No.1 and No.2 were considered obviously better than sample No. 3. Therefore, as a conclusion, it is reasonable to apply gas shrouding to APS process for effectively improving the HER performance of Ni-based electrodes for alkaline electrolyzer.

4 Conclusions

Dual layer coatings were obtained in this work by applying different spray conditions: vacuum, with gas shrouding and without gas shrouding. Gas shrouded APS was carried out through a shrouding head consisted of 12-arranged shrouding nozzles for protecting the plasma plume. Both experimental and numerical results showed that the shrouding gas was able to restrain the entrainment of oxygen and to retain the oxygen fraction on the centreline of plasma plume at low level in the protected region. The plasma plume was surrounded by the shrouding gas and forced to become radially wider and axially shorter which were successfully experimentally and numerically proved. Significant effects of gas shrouding on coating characteristics have been watched to retain more Al in the coatings while reducing the oxygen fraction. The use of gas shrouding should be optimized to achieve gas shield with enough momentum while without bringing too much reduction to the plasma temperature. The shrouding effect was also verified by the electrochemical test that with gas shrouding the performance of electrode was obviously improved close to that of the VPS sprayed electrode.

Acknowledgements

The Ministry of Finance and Economics (MFW) of Baden-Württemberg is gratefully acknowledged for funding the project “Leuchtturmprojekt Power-to-Gas”. The Authors also thanks Günter Roth and Ina Plock for their professional supports during the experiment and the sample characterization.

1. Chen, L., Dong, X., Wang, Y., and Xia, Y. Separating Hydrogen and Oxygen Evolution in Alkaline Water Electrolysis using Nickel Hydroxide. *Nat. Commun.*, 2016, **7**, p 11741–11748.

2. S. Marini, P. Salvi, P. Nelli, R. Pesenti, M. Villa, M. Berrettoni, G. Zangari, and Y. Kiros, Advanced Alkaline Water Electrolysis, *Electrochim. Acta*, 2012, **82**, p 384–391.

3. C.K. Kjartansdóttir, L.P. Nielsen, and P. Møller, Development of Durable and Efficient Electrodes for Large-Scale Alkaline Water Electrolysis, *Int. J. Hydrog. Energ.*, 2013, **38**(20), p 8221–8231.

4. R.L. LeRoy, Industrial Water Electrolysis: Present and Future, *Int. J. Hydrog. Energ.*, 1983, **8**(6), p 401–417.

5. M. Wang, Z. Wang, X. Gong, and Z. Guo, The Intensification Technologies to Water Electrolysis for Hydrogen Production – A Review, *Renew. Sust. Energ. Re.*, 2014, **29**, p 573–588.

6. D. Pletcher and X. Li, Prospects for Alkaline Zero Gap Water Electrolysers for Hydrogen Production, *Int. J. Hydrog. Energ.*, 2011, **36**(23), p 15089–15104.

7. X. Tang, L. Xiao, C. Yang, J. Lu, and L. Zhuang, Noble Fabrication of Ni–Mo Cathode for Alkaline Water Electrolysis and Alkaline Polymer Electrolyte Water Electrolysis, *Int. J. Hydrog. Energ.*, 2014, **39**(7), p 3055–3060.

8. T. Rauscher, C.I. Müller, A. Schmidt, B. Kieback, and L. Röntzsch, Ni–Mo–B Alloys as Cathode Material for Alkaline Water Electrolysis, *Int. J. Hydrog. Energ.*, 2016, **41**(4), p 2165–2176.

9. S.H. Zhou, Y. Wang, L.-Q. Chen, Z.-K. Liu, and R.E. Napolitano, Solution-Based Thermodynamic Modeling of the Ni–Al–Mo System Using First-Principles Calculations, *Calphad*, 2014, **46**, p 124–133.

10. M. Manazoğlu, G. Hapçı, and G. Orhan, Electrochemical Deposition and Characterization of Ni-Mo Alloys as Cathode for Alkaline Water Electrolysis, *J. Mater. Eng. Perform.*, 2016, **25**(1), p 130–137.

11. G. Schiller and V. Borck, Vacuum Plasma Sprayed Electrodes for Advanced Alkaline Water Electrolysis, *Int. J. Hydrog. Energ.*, 1992, **17**(4), p 261–273.

12. G. Schiller, R. Henne, and V. Borck, Vacuum Plasma Spraying of High-Performance Electrodes for Alkaline Water Electrolysis, *J. Therm. Spray Techn.*, 1995, **4**(2), p 185–194.

13. C.H. Chang and J.D. Ramshaw, Computational Study of High-Speed Plasma Flow Impinging on an Enthalpy Probe, *Plasma Chem. Plasma P.*, 1996, **16**(1), p 17–38.

14. J.R. Fincke, C.H. Chang, W.D. Swank, and D.C. Haggard, Entrainment and Demixing in Subsonic Thermal Plasma Jets: Comparison of Measurements and Predictions, *Int. J. Heat Mass Tran.*, 1994, **37**(11), p 1673–1682.

15. M. Brossa and E. Pfender, Probe Measurements in Thermal Plasma Jets, *Plasma Chem. Plasma P.*, 1988, **8**(1), p 75–90.

16. A. Capetti and E. Pfender, Probe Measurements in Argon Plasma Jets Operated in Ambient Argon, *Plasma Chem. Plasma P.*, 1989, **9**(2), p 329–341.

17. M. Rahmane, G. Soucy, and M. Boulos, Analysis of the Enthalpy Probe Technique for Thermal Plasma Diagnostics, *Rev. Sci. Instrum.*, 1995, **66**(6), p 3424–3431.

18. T. Liu and J. Arnold, Study of in-Flight Particle Stream and Particle Behaviour for Understanding the Instability Phenomenon in Plasma Spraying Process, *Surf. Coat. Tech.*, 2016, **286**, p 80–94.

19. G.K. Batchelor, *An Introduction to Fluid Dynamics*, Cambridge University Press, 2000, p 131-173, doi:10.1017/CBO9780511800955.005.

20. N. Phan-Thien, *Understanding Viscoelasticity: An Introduction to Rheology*, N. Phan-Thien, Ed., Springer Berlin Heidelberg, 2013, p 1–27, doi:10.1007/978-3-642-32958-6_1.

21. B.E. Launder and D.B. Spalding, The Numerical Computation of Turbulent Flows, *Comput. Method. Appl. M.*, 1974, **3**(2), p 269-289.

22. D. Miousse, A. Lasia, and V. Borck, Hydrogen Evolution Reaction on Ni-Al-Mo and Ni-Al Electrodes Prepared by Low Pressure Plasma Spraying, *J. Appl. Electrochem.*, 1995, **25**(6), p 592–602.

23. G.D. Short and E. Bishop, Concentration Overpotentials on Antimony Electrodes in Differential Electrolytic Potentiometry, *Anal. Chem.*, 1965, **37**(8), p 962–967.

24. I. Herraiz-Cardona, E. Ortega, J.G. Antón, and V. Pérez-Herranz, Assessment of the Roughness Factor Effect and the Intrinsic Catalytic Activity for Hydrogen Evolution Reaction on Ni-Based Electrodeposits, *Int. J. Hydrog. Energ.*, 2011, **36**(16), p 9428–9438.

25. C. Kjartansdóttir, M. Caspersen, S. Egelund, and P. Møller, Electrochemical Investigation of Surface Area Effects on PVD Al-Ni as Electrocatalyst for Alkaline Water Electrolysis, *Electrochim. Acta*, 2014, **142**, p 324–335.

26. T. Shinagawa, A.T. Garcia-Esparza, and K. Takanabe, Insight on Tafel Slopes from a Microkinetic Analysis of Aqueous Electrocatalysis for Energy Conversion, *Sci. Rep.*, 2015, **5**, doi:10.1038/srep13801.

27. G.S. Tasic, S.P. Maslovara, D.L. Zugic, A.D. Maksic, and M.P. Marceta Kaninski, Characterization of the Ni–Mo Catalyst Formed in Situ during Hydrogen Generation from Alkaline Water Electrolysis, *Int. J. Hydrog. Energ.*, 2011, **36**(18), p 11588–11595.

28. Y.H. Fang and Z.P. Liu, Tafel Kinetics of Electrocatalytic Reactions: From Experiment to First-Principles, *ACS Catal.*, 2014, **4**(12), p 4364–4376.

29. D.S. Hall, D.J. Lockwood, C. Bock, and B.R. MacDougall, Nickel Hydroxides and Related Materials: A Review of Their Structures, Synthesis and Properties, *P. Roy. Soc. A-Math. Phy.*, 2015, **471**(2174), doi:10.1098/rspa.2014.0792.

30. S. Fletcher, Tafel Slopes from First Principles, *J. Solid State Electr.*, 2009, **13**(4), p 537–549.